

Atom Tunneling in the Water Formation Reaction $\text{H}_2 + \text{OH} \rightarrow \text{H}_2\text{O} + \text{H}$ on an Ice Surface

Jan Meisner,^{*} Thanja Lamberts, and Johannes Kästner

Institute for Theoretical Chemistry, University of Stuttgart, Pfaffenwaldring 55, 70569 Stuttgart, Germany

E-mail: meisner@theochem.uni-stuttgart.de

December 5, 2021

Abstract

OH radicals play a key role as an intermediate in the water formation chemistry of the interstellar medium. For example the reaction of OH radicals with H_2 molecules is among the final steps in the astrochemical reaction network starting from O, O_2 , and O_3 . Experimentally it was shown that even at 10 K this reaction occurs on ice surfaces. As the reaction has a high activation energy only atom tunneling can explain such experimental findings.

In this study we calculated reaction rate constants for the title reaction on a water-ice I_h surface. To our knowledge, low-temperature rate constants on a surface are not available in the literature. All surface calculations were done using a QM/MM framework (BHLYP/TIP3P) after a thorough benchmark of different density functionals and basis sets to highly accurate correlation methods. Reaction rate constants are obtained using instanton theory which takes atom tunneling into account inherently, with constants down to 110 K for the Eley–Rideal mechanism and down to 60 K for the Langmuir–Hinshelwood mechanism. We found that the reaction is nearly temperature independent below 80 K. We give kinetic isotope effects for all possible deuteration patterns for both reaction mechanisms. For the implementation in astrochemical networks, we also give fit parameters to a modified Arrhenius equation. Finally, several different binding sites and binding energies of OH radicals on the I_h surface are discussed and the corresponding rate constants are compared to the gas-phase case.

Keywords: *astrochemistry, interstellar medium molecules, water formation, kinetics, tunneling, isotopes*

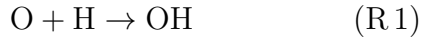
Introduction

Water ice was first detected in 1973¹ and is meanwhile known to be the main component of most interstellar ices.^{2–4} Therefore, the surface formation of water in space was studied extensively experimentally in ultra-high vacuum setups^{5–15} and through modeling studies with

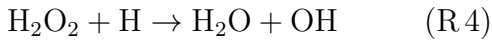
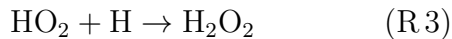
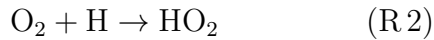
different varieties of Kinetic Monte Carlo^{16–21} and rate equation models.^{22–24} Although water can also be formed via gas-phase reactions, it is the formation on the surface of dust grains in dense molecular clouds that can explain the observed abundances. One of the crucial factors is that the surface provides an efficient way for the reaction products to lose their excess energy.²⁵ In other words, addition reactions which yield only one reaction product cannot take place in the gas phase, but can take place on the surface. For more insight on the gas-phase

routes we refer the reader to the recent review by Van Dishoeck *et al.*²⁶ and focus on surface chemistry from hereon. An involved network of surface reactions in the interstellar medium (ISM) was originally proposed by Tielens and Hagen²⁷ and has been updated incorporating the experimental results mentioned above.^{13,21} Three main water formation routes constitute this network: hydrogenation of atomic oxygen, molecular oxygen (O_2), and ozone (O_3). Depending on the interstellar region of interest different routes dominate. In each pathway the hydroxyl radical is formed and subsequently reacts with either atomic or molecular hydrogen.

The barrierless direct hydrogenation of O atoms by H atoms is believed to be important in translucent and diffuse clouds in which H atoms are more abundant than H_2 molecules¹⁶ and was experimentally studied by different groups.^{5,28,29}



Alternatively, O_2 can be hydrogenated twice and the resulting hydrogen peroxide (H_2O_2) reacts with another H atom to form water and a hydroxyl radical:



These reactions have been shown to proceed even at temperatures as low as 12 K.^{6,7,10} The last reaction again proceeds via a barrier and has been shown to take place via tunneling both experimentally¹² and using instanton theory.³⁰ Note that the sequential hydrogenation of O_2 up to H_2O_2 is not possible in the gas phase, because of the reasons mentioned above. The reaction between H and HO_2 can also result in two OH radicals via a decomposition of activated $H_2O_2^*$ ^{31,32}

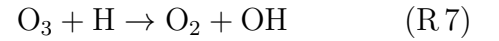


The resulting OH radicals can recombine to H_2O_2 or form water and an O atom:

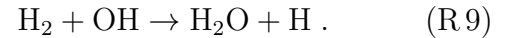
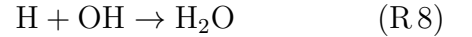


Microscopic kinetic Monte Carlo modeling found that experiments can be best described by the sequence R2, R3 leading to $H_2O_2^*$ and R5 with OH radical recombination to H_2O_2 dominating over reaction R6.^{21,33}

Finally, O_3 can be hydrogenated which leads to an O_2 molecule and OH radical and has been experimentally studied in the solid state at 10 K.^{11,34}



In all of these reaction pathways, OH radicals are formed. Subsequent reaction to form water can take place via reaction R8 or R9:



Reaction R8 is barrierless, since it is a radical recombination reaction, but the reaction with H_2 proceeds via a barrier. It is the topic of this paper. A hydrogen atom is transferred from the H_2 molecule to the OH radical to finally form water. In the ISM the competition between reactions R8 and R9 is determined by the interstellar environment, the relative abundances of H, H_2 , and O in the gas phase, and the reaction rates. Modeling this process in dense molecular clouds – where ice layers are thick and the H_2 abundance is high – therefore requires detailed knowledge of the low-temperature reaction rate constant. Reaction (R9) in the gas phase was studied extensively experimentally^{35–37} and computationally.^{38–42} The high activation energy of 2000 K (experimentally determined by laser-induced fluorescence after photolysis)^{36,43} to 3000 K (computationally determined)^{41,42} shows that atom tunneling is crucial for the reaction rate at low temperatures.^{39,41,42} Oba *et al.* found experimental evidence that the reaction of H_2 and OH to wa-

ter and hydrogen atoms also occurs on surfaces even at 10 K due to atom tunneling.⁴⁴ Recently, we published an extensive study on the reaction of molecular hydrogen and hydroxyl radicals (equation (R 9)) in the gas phase including all possible isotope patterns down to 80 K.⁴² Here, we extend this work to the adsorption of OH radicals onto crystalline I_h water ice and the subsequent reaction with H_2 . We present binding sites, energies, reaction paths and reaction rate constants for the reaction of H_2 with OH on the surface. This includes the effect of atom tunneling at low temperatures via the use of instanton theory.

This paper is structured as follows: In the methods section we present a benchmark to find a suitable density functional and basis set by comparing the quality with highly correlated calculations on UCCSD(T)-F12^{45,46} level. Furthermore, the water ice surface and the organization of the QM/MM setup, as well as the methodology of the reaction rate calculations are described. In the results section we show binding sites and binding energies of the OH radical on the ice surface as well as accompanying activation energies, transition state structures and intrinsic reaction coordinates (IRC). We give reaction rate constants for the Eley-Rideal and the Langmuir-Hinshelwood mechanism using multidimensional atom tunneling via semiclassical instanton theory⁴⁷⁻⁵¹ and make a comparison to the analytical solution of an Eckart shaped barrier. The results are compared to those in the gas phase and the impact of surfaces on the reactivity is discussed. Kinetic isotope effects for all eight possible permutations of exchanging hydrogen for deuterium are shown as well. The last section discusses the implications to astrochemistry, gives fits of to a modified Arrhenius equation and concludes the study.

Methods

Choice of Electronic Potential

In order to obtain reliable reaction rate constants, the method to calculate the underlying electronic potential has to be as accurate as possible. Instanton calculations using highly correlated wave function methods are too time consuming so we applied density functional theory (DFT) throughout this work. For this purpose, an extensive benchmark of the most common functionals and basis sets has been performed, as can be seen in the Supplementary Information. The BHLYP functional⁵²⁻⁵⁶ in combination with the def2-SVPD basis set⁵⁷ is found to describe the reaction well. The BHLYP functional has previously been found to describe astrochemical reactions with open-shell molecules properly.^{58,59} It was also found appropriate for water-water interactions (see Supplementary Information). Thus BHLYP is used in the remainder of this paper. All DFT calculations were performed with Turbomole version 7.0.⁶⁰ SCF energies were converged to an accuracy of 10^{-9} Hartree on an $m5$ grid.⁶¹

To include the environment, *i.e.*, the water surface, we used a QM/MM framework for which we used the ChemShell interface.^{62,63} The QM part can be polarized by means of electrostatic embedding into the MM charges. All geometry optimizations and reaction rate calculations were done with DL-FIND.⁶⁴ The visualization of the molecules and ice surface was done using Visual Molecules Dynamics (VMD).⁶⁵

Surface Model and QM/MM setup

We used the (0001) surface of hexagonal ice I_h that minimizes the surface free energy as described by Fletcher.⁶⁶ The structure of the bare surface can be seen in Fig. 1. In that phase, the protons are ordered. Equivalent sites for rows (vertical in the top image in Fig. 1). While the majority of solid water in the ISM is expected to be amorphous, the crystalline phase is easier to model because only a limited number of distinct adsorption sites is available.

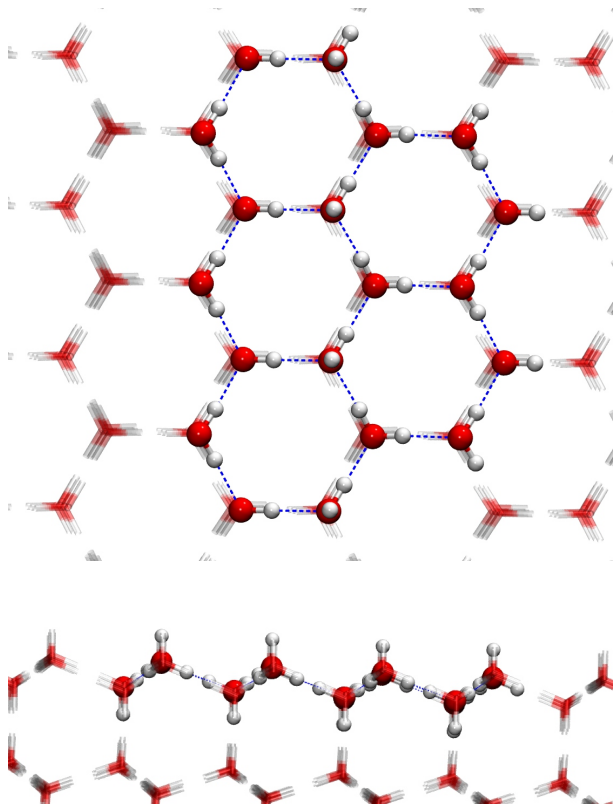


Figure 1: QM/MM setup of the Fletcher surface. The solid ball-and-stick-molecules represent the QM region while the transparent ones represent the MM region. All MM water molecules within a radius of 15 Å are allowed to move and rotate.

The structural model consisted of a hemisphere with a radius of 25 Å comprising 1151 water molecules. The MM part was described by the TIP3P potential.⁶⁷ For the QM part, we used five adjoining water hexagons of the top layer: 19 water molecules and the adsorbed atoms. Geometry optimisations included all water molecules within a radius of 15 Å around the center of the hemisphere (261 molecules) as active atoms, the other H₂O molecules were frozen. This leads to a proton disordering of the surface. All in all, 2349 variables are to be optimised for the bare surface. Instantons and the corresponding Hessians have been calculated with a reduced dimensionality: here, only the adsorbed atoms/molecules and the hexagon of six closest water molecules were flexible.

Reaction Rate Calculations and Tunneling

To calculate reaction rate constants including atom tunneling we use instanton theory,^{68–77} a method based on Feynman’s path integrals,⁷⁸ which is increasingly used⁷⁹ to calculate chemical reaction rate constants.^{30,75,80–104} In instanton theory, a closed Feynman path spans the barrier region. At low temperatures it extends towards the reactant state. At temperatures above the crossover temperature

$$T_c = \frac{\hbar\omega_{TS}}{2\pi k_B} \quad (1)$$

the instanton path generally collapses to one single point on the potential energy surface.⁹⁹ Here, \hbar is Planck’s constant divided by 2π , k_B is Boltzmann’s constant and ω_{TS} is the absolute value of the imaginary frequency at the transition state structure in the harmonic approximation. The crossover temperature gives a first and simple estimate at which temperature atom tunneling becomes important. The mass-dependence of ω_{TS} also causes mass-dependence of T_c .

For the reaction on the Fletcher surface, the closed Feynman path was discretized with 40 images down to 175 K and with 78 images down to 80 K. For the gas phase reaction (of all isotopologues), 200 images were used for the whole temperature range. Vibrational modes are included harmonically around the Feynman path. The rotational partition functions of the reactants and the images of the instantons were approximated by those of rigid rotors. The translational partition function was included within the approximation of an ideal gas, which is identical to the quantum particle in a box. The rotational partition function of the whole instanton was calculated to be the geometric mean value of the rotational partition functions of all images. The symmetry number $\sigma = 2$ was taken into account when calculating the rotational partition function of the H₂ and D₂ molecules for bimolecular reaction rates.¹⁰⁵ For the reactions with HD and for unimolecular reaction rates in general, $\sigma = 1$ was used because the rotation of adsorbed molecular hydrogen is

hindered by the surface.

Besides the structural model which includes the surface atoms explicitly, we alternatively mimic the effect of the ice surfaces on the partition function for reactions calculated in a gas-phase model in an approach we successfully applied previously.¹⁰³ For unimolecular reaction rate constants, the rotational partition function is assumed to be constant during the reaction just as the surface suppresses the rotation in the reactant as well as in the transition state. For bimolecular reaction rate constants, only the translation and rotation of the H₂ fragment is considered in the reactant state. Rotational and translational motion of the OH radical and transition state structure are suppressed, just as it is the case when OH is adsorbed on the surface. It has to be mentioned that while this approach properly approximates the suppressed motion of the species on the surface, it neglects any influence of the surface on the potential energy along reaction path and therefore the corresponding potential activation energy. Hereinafter, this methodology is referred to as *implicit surface model*.

Instantons were considered to be converged when all components of the nuclear gradient are smaller than $1 \cdot 10^{-8}$ a.u.. Instanton calculations were performed at temperatures below the crossover temperature of $280 \text{ K} \pm 5 \text{ K}$ (depending on the binding site). Because of the existence of a pre-reactive minimum, below a particular, mass-dependent temperature, the tunneling energy is lower than the potential energy of the separated products for bimolecular reaction rates. At that temperature, canonical instanton theory becomes unreliable.¹⁰⁶ Therefore, bimolecular reaction rates can only be provided for 110 K and higher temperatures for the reaction $\text{H}_2 + \text{OH} \rightarrow \text{H} + \text{H}_2\text{O}$.

Calculations of intrinsic reaction coordinates (IRCs) have been performed using a modified version of Schlegel’s Hessian-Predictor-Corrector method^{107–109} with a step size of 0.05 mass-weighted atomic units.

Results

Binding Sites and Energies

We identified three different binding sites of OH on the Fletcher surface, which are shown in Fig. 2. We calculated the corresponding adsorption energies with and without harmonically approximated vibrational zero-point energies. The values are given in table 1. For all binding sites, zero-point energy reduces the binding energy by around 16 kJ mol^{-1} (1920 K) because the OH–surface complex has additional vibrational modes. The harmonic approximation can be assumed to overestimate the zero-point energy which leads to an underestimation of the corresponding adsorption energy.

In the first binding site, the OH radical is located directly in the middle of a water hexamer where it accepts hydrogen bonds from two of the dangling hydrogen atoms and donates a hydrogen bond to the O atom of a water molecule of the surface. We call this binding site *hollow*. The binding energy is 40.5 kJ mol^{-1} (4870 K) including zero-point energy.

In a similar binding site the OH radical is also hydrogen-bound to the oxygen atom of a water molecule and to one dangling hydrogen atom of the surface, see Fig. 2. The third hydrogen bond is absent, *i.e.*, the OH radical bridges two surface water molecules. We call this binding site *bridged*. As this binding site is rather similar to the *hollow* one, the binding energy is with 39.7 kJ mol^{-1} (4770 K) only slightly smaller.

In the third binding site the OH radical is located on top of one of the water molecules. Because of that we call this binding site *top*. The OH radical also accepts two hydrogen bonds from the surface and donates one. The binding energy of this site is with 32.1 kJ mol^{-1} (3860 K) lower than for the *hollow* and *bridged* binding sites. These values lie nicely in the range of experimentally determined desorption energies on silicate surfaces of 1656–4760 K.¹¹⁰

Reaction Barriers

One possibility for the reaction of the OH radical with molecular hydrogen on the ice surface

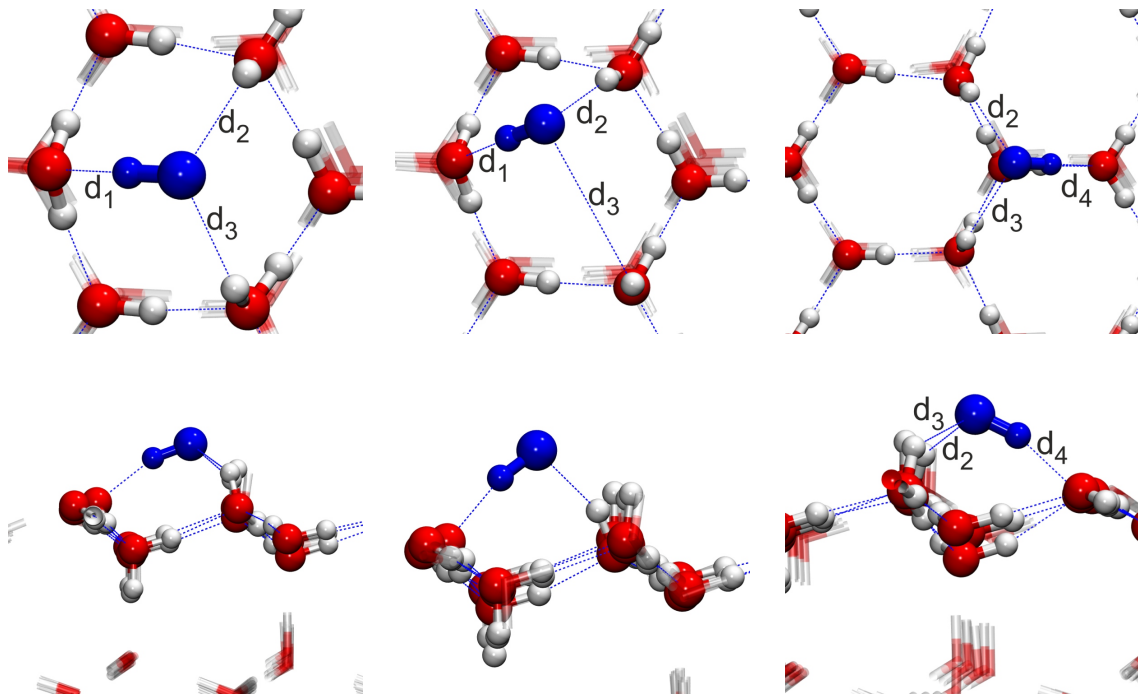


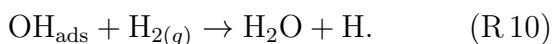
Figure 2: Structures of the adsorbed OH radical (blue) on the Fletcher surface. All binding sites are shown from top and side perspectives. Left: *Hollow*, Middle: *Bridged*, Right: *Top*

Table 1: Adsorption energies of OH on the Fletcher surface and hydrogen bond distances. V_{ads} and E_{ads} denote the adsorption energy without and with zero point energy, respectively. The hydrogen-bond lengths d_1 to d_4 are explained in Fig. 2. Energies are given in kJ mol^{-1} , distances in \AA .

	V_{ads}	E_{ads}	d_1	d_2	d_3	d_4
Hollow	57.0	40.5	1.77	2.22	2.27	
Bridged	55.6	39.7	1.77	1.99	3.89	
Top	48.1	32.1		2.11	2.36	1.78

is the Eley–Rideal (ER) mechanism, in which one species is adsorbed on the surface and the other one is approaching from the gas phase.

We have shown that the binding energy of OH radicals is much higher than the binding energy of H_2 molecules ($3.6\text{--}4.6\text{ kJ mol}^{-1}$; $440\text{--}555\text{ K}$).¹¹¹ Therefore, we first investigate the reaction of adsorbed OH radicals with H_2 molecules directly from the gas phase:



In this work, we restrict ourselves to the chemical reaction forming H_2O molecules and ignore the physical processes after that. Therefore, for the products the label indicating the aggregate state was omitted. For each binding site of OH we found one corresponding transition state structure. These transition state structures are called *direct* hereinafter. The vibrational adiabatic reaction barriers with respect to the separated reactants (potential energy barriers including zero-point energy) of these transition state structures lie between 24.2 and 24.7 kJ mol^{-1} , (2910 and 2970 K), see table 2. This is just slightly lower than the adiabatic reaction barrier of the gas phase reaction of 25.4 kJ mol^{-1} (3055 K , from separated reactants). Here we want to stress that all reaction barriers are very similar, independently of the corresponding adsorption energies, although the latter vary over 8 kJ mol^{-1} . This is in agreement with what is found for reactions on amorphous solid water.¹⁰¹

We found another type of transition state structures in which the hydrogen atom of the OH radical points away from the surface and the H_2 molecule approaches via a path closer

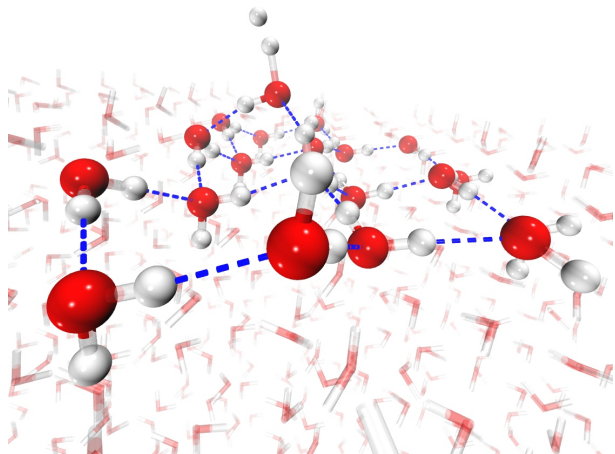


Figure 3: Transition state structure of the *direct-hollow* binding site. QM atoms are shown as balls and sticks, MM atoms as transparent sticks.

to the surface. The $[\text{OH} \cdots \text{H}_2]$ complex possesses similar internal coordinates as in the *direct* transition state structures but is rotated with respect to the ice surface. For these *rotated* transition state structures, the adiabatic reaction barriers are 49.3 and 45.7 kJ mol^{-1} (5930 K and 5500 K) for the *hollow* and the *top* binding site, respectively. No *rotated* transition state structure was found for the *bridged* binding site. Since the barriers via *rotated* transition states are much higher than those via the *direct* transition states, the latter have result in much higher rates and the former are not considered further.

We calculated the potential energy along the intrinsic reaction coordinates (IRCs) of the different binding sites. The end of the IRCs define pre-reactive complexes (PRCs). Those are geometries in which an H_2 molecule is loosely bound to the surface in the vicinity of the OH radical. These structures are used as reactant states to calculate the unimolecular activation energies shown in table 2.

The potential energy curves along the IRCs belonging to the different binding sites are almost indistinguishable from the one of the gas-phase reaction, see Fig. 4. This shows again that the surface has negligible influence on the potential energy along the reaction path. Dur-

Table 2: Reaction barriers including zero-point energies. The label *bi* denotes that the barrier is given with respect to the separated reactants, *i.e.*, $\text{OH}_{(ads)}$ and $\text{H}_{2(g)}$. The label *uni* indicates barriers with respect to the respective pre-reactive complexes. All values are in kJ mol^{-1} .

	Hollow	Bridged	Top	Gas Phase
$E_{A,bi}^{\text{direct}}$	24.2	24.7	24.3	25.4
$E_{A,bi}^{\text{rotated}}$	49.3	—	45.7	—
$E_{A,uni}^{\text{direct}}$	22.5	24.1	22.4	24.4

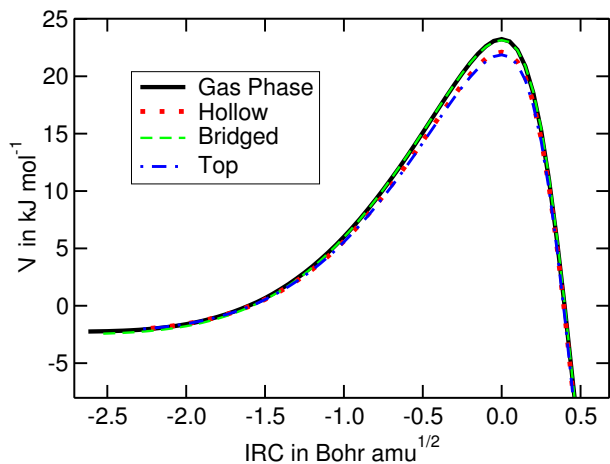


Figure 4: Above: Potential energy V of the intrinsic reaction coordinates (IRCs) of the *hollow*, *top*, and the *bridged* binding site compared with the gas-phase reaction.

ing the reaction, any changes in the hydrogen bond length remain below 0.2 Å, see Fig. S3 of the Supplementary Information. Overall, a classical catalytic effect is absent: the activation barrier is unaltered, neither is the reaction mechanism changed. This can be explained by the adsorption energy during the reaction. In typical heterogeneous catalysis the molecules are activated through interactions with the surface in a way that the energy of the transition state with respect to the energy of the reactant state is reduced. These interactions are either forming new chemical bonds or causing a shift in electron density. In our case, the OH radical forms three hydrogen bonds in the adsorption

Table 3: Geometric parameters of the transition state structures for different binding sites in comparison to the gas phase transition state structure. The O–H distance of the newly formed bond, the H–H distance of the original H₂ molecule, and the H–O–H angle of the newly formed water molecule are denoted by $d_{\text{O-H}}$, $d_{\text{H-H}}$, and $\angle(\text{H-O-H})$, respectively. Distances are in Å and angles in degrees.

	$d_{\text{O-H}}$	$d_{\text{H-H}}$	$\angle(\text{H-O-H})$
Hollow	1.33	0.83	99.2
Top	1.33	0.83	99.7
Bridged	1.33	0.84	98.7
Gas phase	1.36	0.82	96.8

process and these three hydrogen bonds are retained during the whole reaction. Therefore, the adsorption energies of the reactant state and the transition state structure are virtually the same and the potential energy of the reaction remains comparable to the gas phase. Reaction with an OH radical bound via four hydrogen bonds is impossible due to steric hindrance. Therefore, the maximal number of H-bonds to a reactive OH is always three, independent of the existence of *e.g.* cavities for surface defects. It can, therefore, be assumed that amorphous solid water ices behave similarly in terms of negligible catalytic effect.

Note, that any processes after the formation of the chemical bonds, like desorption or dissipation, are outside of the scope of this article because they do not influence the rate. The kinetic bottleneck in the water formation from H₂ molecules and OH radicals is the H–H bond breaking which is described here.

Reaction Rate Constants for the Eley–Rideal Mechanism

In the Eley–Rideal (ER) mechanism, one particle (a molecule or an atom) physisorbs on the surface and thermalizes there. Another particle comes and directly reacts with the pre-adsorbed

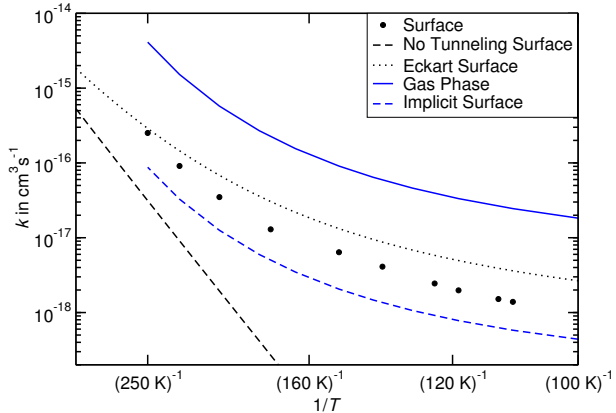


Figure 5: Arrhenius plot of the bimolecular (Eley–Rideal) reaction rate constants. Instanton theory is used if not stated otherwise. Surface reaction rates are calculated for the *direct-hollow* reaction path.

particle to form the products. In this study, we want to focus on reaction (R10) where an OH radical is adsorbed and the H₂ molecule comes in from the gas phase, since OH has a higher adsorption energy. The incoming H₂ molecule reacts with the OH-surface system in what can be formally seen as a bimolecular reaction. Instantons were calculated from 250 K to 110 K. For comparison, we calculated reaction rate constants using the approximation of an Eckart-shaped barrier.

As the reaction profiles of all three *direct* transition state structures and IRCs are nearly identical, we only calculated reaction rate constants of the *direct-hollow* transition state structure. Due to high computational costs the active region for the instanton calculations was reduced to the one water hexamer below the adsorbed OH radical. The resulting adiabatic activation energy of 24.11 kJ mol^{−1} almost equal to the 24.19 kJ mol^{−1} obtained for the full active region.

The resulting reaction rate constants are compared to the gas-phase data calculated on the same potential energy surface in the Arrhenius plot in Fig. 5. The rate constants including tunneling correction via the Eckart barrier and those obtained by transition state theory without tunneling are shown for comparison. The implicit surface model is able to reproduce the

rate constants of the explicit surface calculations up to factors of 3.6 and 2.7 at 275 K and 110 K, respectively. This indicates that for reactions without a classical catalytic effect, the implicit surface approach is a promising approximation. Numeric values for the rate constants are available in the Supplementary Information, table S II.

Reaction Rate Constants for the Langmuir–Hinshelwood Mechanism

In the Langmuir–Hinshelwood (LH) mechanism, both particles are adsorbed on the surface and diffuse until they meet. If they approach each other, they form a PRC. This PRC can either react or decay by diffusion or desorption of one or both reactants. The reaction of a PRC to the products is a unimolecular process. Thus, Langmuir–Hinshelwood reactions are characterized by unimolecular rate constants.

We calculated unimolecular reaction rate constants for the *hollow* binding site. The adiabatic activation barriers for the LH mechanism in all binding sites are given as $E_{A,\text{uni}}^{\text{direct}}$ in table 2. The resulting unimolecular rate constants k_{react} are shown in Fig. 6 and table S II. Instantons were calculated down to 80 K. At even lower temperatures, more images would be required to obtain converged reaction rates which would render the computations too expensive.

The rate constants from the implicit surface model agree within one order of magnitude with those from the full ice surface model, see Fig. 6.

The main effects of a surface on catalysis are

1. An increase in the concentration of reactive species compared to the gas phase, especially in low-pressure environments like the ISM.
2. The removal of excess heat of reaction and, thus, the stabilization of reaction products of exothermic reactions.
3. Restricted mobility, in particular rotation.

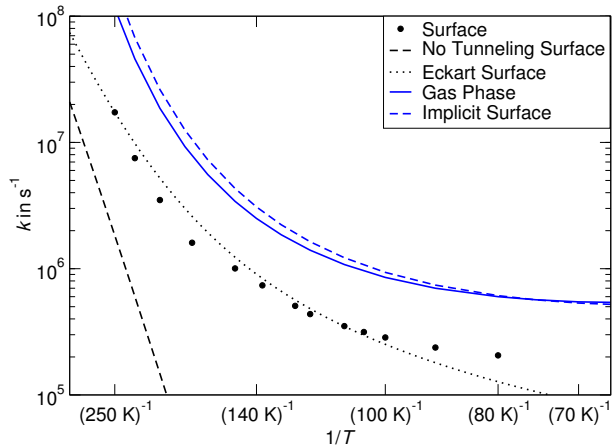


Figure 6: Arrhenius plot of the unimolecular Reaction rate constants. Surface reaction rates were calculated around the direct-hollow reaction pathway.

4. Alternations of the barrier height and possibly the reaction path, *i.e.*, a classical catalytic effect.

In any atomistic models based on transition state theory, as used in the present work, effects (1) and (2) are included implicitly. Rate constants are independent of the concentrations. Thermal rate constants assume a canonic ensemble, *i.e.*, thermal equilibrium throughout the reaction. Excess heat is removed instantly. The implicit surface model we propose here also includes (3), the immobilization. Only (4), the classical catalytic effect, is neglected by the implicit model, but taken into account in an explicit surface model in which the surface atoms are actually included in the structural model.

The results of the standard gas-phase model and the gas-phase calculations using the implicit surface model are closer for the unimolecular reaction than for the bimolecular calculations. The reason is that in the unimolecular case, the implicit surface model merely assumes that the rotational partition function of the PRC is the same as the one of the transition state (*e.g.* that both do not rotate), while their rotation is taken into account in the gas phase. As both PRC and transition state have similar rotational partition functions (they include the same atoms), the neglect of this term is of minor effect. In the bimolecular case, the

implicit surface model removes translation and rotation of one reactant (OH) and the transition state, which is a much larger alternation of the rate constant. Note, that due to the inhibited rotation of the H_2 molecule in the PRC the symmetry number $\sigma = 1$ was used for the explicit and implicit surface calculations.

Kinetic Isotope Effects

We used the implicit surface model to calculate kinetic isotope effects (KIEs) for all eight possible deuteration patterns. Bimolecular and unimolecular reaction rate constants are shown in Fig. 7 and Fig. 8, respectively. When substituting protium atoms with deuterium atoms, the crossover temperature reduces significantly as a result of a smaller imaginary frequency and therefore a smaller crossover temperature. Thus, the rate constants are reported here for 200 K and below. For bimolecular reaction rates, the temperature below which the tunneling energy is lower than the potential energy of the asymptotic reactants changes with the mass, too. Here and in Fig. 7 and Fig. 8 the isotope patterns are labeled as in our previous work⁴² as $\text{H}^1\text{H}^2\text{OH}^3$ such that the reaction reads $\text{H}^1\text{H}^2 + \text{OH}^3 \rightarrow \text{H}^1 + \text{H}^2\text{OH}^3$. DDOH therefore corresponds to a reaction of OH with D_2 while HDOH corresponds to the reaction $\text{HD} + \text{OH} \rightarrow \text{H} + \text{DOH}$.

In both, the bimolecular and unimolecular cases, the primary KIE – the ratio between the rate constants of H-transfer and the corresponding D-transfer – is as big as two orders of magnitude but also depends on the isotope pattern of the other two hydrogen atoms.

For the bimolecular case, the KIEs are similar to the ones reported in the gas phase.⁴² The secondary KIEs play a smaller role as they are in all cases smaller than 10. When substituting OH by OD, an inverse KIE is found, *i.e.*, the rate constant increases due to deuteration. This small inverse secondary KIE, about 2–3 is caused by differences in the zero-point energy.^{112–115} The inverse KIE for the deuteration of OH was also present in the gas-phase reaction rate constants where the difference in zero-point energy corrected activation barrier between the

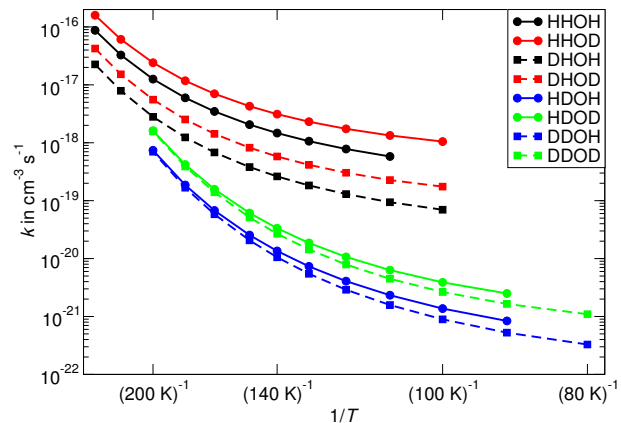


Figure 7: Temperature dependence of the (bi-molecular) Eley-Rideal reaction rate constants of all H/D isotopologues calculated with the instanton method and the implicit surface approximation.

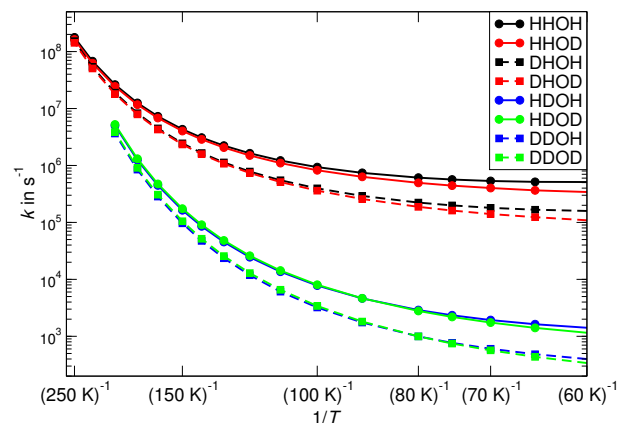


Figure 8: Temperature dependence of the unimolecular rate constants of all H/D isotopologues, which can be used to calculate R_{LH} calculated with the instanton method and the implicit surface approximation.

HHOH and the HHOD system is 1.3 kJ mol^{-1} (156 K).⁴²

In the unimolecular case, the primary KIEs are ≈ 5 at 200 K and increase to ≈ 300 at 60 K. The secondary KIEs play an even smaller role than in the bimolecular case and no inverse KIE is present, see Fig. 8.

Astrochemical Implications

In order to provide our calculated rate constants to astrochemical modelers in an easily implementable way, we have fitted all curves in Figs. 7 and 8 to the following analytical expression:¹¹⁶

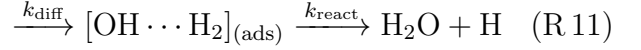
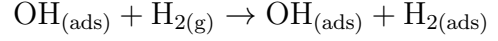
$$k(T) = \alpha \left(\frac{T}{300 \text{ K}} \right)^\beta \exp \left(-\gamma \frac{T + T_0}{T^2 + T_0^2} \right) \quad (2)$$

Here, the parameters α , β , γ , and T_0 are all fitting parameters, where α has the units of the rate constant, β regulates the low-temperature behavior, and γ and T_0 can be related to the activation energy of the reaction. To obtain a realistic low-temperature extrapolation the value of β has been fixed to 1. For the fitting procedure we use the Eckart approximation above the crossover temperature, equation (1), and the values calculated with instanton theory below T_c . The exact values for the fit parameters for all eight isotope-substituted reactions are given in the Supplementary Information along with the corresponding reaction rate constants.

We have found that the energy barrier is rather independent of the binding site. We have found the same trend for the reaction of HNC O with hydrogen atoms on amorphous solid water.¹⁰¹ Furthermore, from the figures in the previous Section it is apparent that the curves of the rate constants flatten off with decreasing temperature. Therefore, in order to be able to use our unimolecular rate constants in models that take the very low temperatures in dense molecular clouds (20 K) into account, we recommend to use the value of the rate constant at the lowest temperature given (60 K) with an approximate error bar of \pm half an order of magnitude.

As mentioned above, there is a relation between bimolecular rate constants and the Eley–Rideal mechanism and unimolecular rate constants and the Langmuir–Hinshelwood mechanism. Given the typical low fractions of OH radicals available at the surface for direct H_2 impingement,^{21,117} the Langmuir–Hinshelwood mechanism where two species find each other via surface diffusion is expected to dominate.

The Langmuir–Hinshelwood mechanism can be described as a reaction cascade:



Diffusion forms the pre-reactive complex (PRC), which reacts to the products. The reaction rate of the last step is $R_{\text{react}} = k_{\text{react}} n([\text{OH} \cdots \text{H}_2]_{(\text{ads})})$, *i.e.*, a unimolecular process with the rate constant k_{react} . The rate of the overall LH process, R_{LH} , can be expressed as the probability to react, P_{react} , multiplied by the rate at which the particles meet, R_{diff} :

$$R_{\text{LH}} = P_{\text{react}} R_{\text{diff}} \quad (3)$$

$$= P_{\text{react}} \frac{k_{\text{diff,H}_2} + k_{\text{diff,OH}}}{N_{\text{sites}}} n(\text{H}_2) n(\text{OH}) \quad (4)$$

The overall process is bimolecular, of course. It depends on the surface concentrations $n(\text{H}_2)$ and $n(\text{OH})$, as well as on the concentration of adsorption sites N_{sites} .

When surface diffusion and microscopic sites are not explicitly included in the model, such as is commonly the case for two-, three- or multiphase rate-equation models, the competition between reaction, diffusion, and desorption of the reactants after they reside next to each other has to be taken into account. This can be done by calculating the probability to react as the ratio between the rate constant for reaction and the total rate constant for all processes:

$$P_{\text{react}} = \frac{k_{\text{react}}}{k_{\text{react}} + k_{\text{diff,H}_2} + k_{\text{diff,OH}} + k_{\text{des,H}_2} + k_{\text{des,OH}}} \quad (5)$$

With this formulation of a LH rate, two limiting cases can be discussed. In both, we will assume for simplicity that the desorption is negligible compared to reaction and diffusion. The first case is a diffusion-limited reaction, in which the diffusion of both species is much slower than the reaction ($k_{\text{diff}} \ll k_{\text{react}}$). Then

Table 4: Reaction rate constants k in $\text{cm}^3 \text{s}^{-1}$ and kinetic isotope effects for low- T unimolecular reactions with different approaches.

Rate constant	Rectangular barrier		Eckart barrier		Instanton theory
	ref 22 [†]	this work [‡]	ref 23 ^a	this work [°]	this work [°]
HHOH	$1.40 \times 10^{+1}$	$6.31 \times 10^{+2}$	$4.07 \times 10^{+5}$	$3.19 \times 10^{+5}$	$5.12 \times 10^{+5}$
DHOH	1.11×10^{-1}	$6.31 \times 10^{+2}$	$3.62 \times 10^{+5}$	$1.16 \times 10^{+5}$	$1.59 \times 10^{+5}$
HDOH	1.11×10^{-1}	9.76×10^{-2}	$1.00 \times 10^{+3}$	$3.12 \times 10^{+2}$	$1.41 \times 10^{+3}$
HHOD	$1.30 \times 10^{+1}$	$6.31 \times 10^{+2}$	$8.74 \times 10^{+5}$	$4.62 \times 10^{+5}$	$3.42 \times 10^{+5}$
DDOH	2.51×10^{-3}	9.76×10^{-2}	$8.07 \times 10^{+2}$	$3.40 \times 10^{+2}$	$3.99 \times 10^{+2}$
KIEs wrt. HHOH					
DHOH	127	1.00	1.12	1.37	3.22
HDOH	127	6465	407	511	363
HHOD	1.08	1.00	0.466	0.69	1.50
DDOH	5578	6265	504	938	1283

[†] $a = 1 \text{ \AA}$, m as the reduced mass, $E_{\text{reaction}} = 2100 \text{ K}$

[‡] $a = 1 \text{ \AA}$, m as the mass of the transferring atom, $E_{\text{reaction}} = 2700 \text{ K}$

[°] at 60 K

^a Literature values²³ multiplied by $\nu_{\text{trial}} = 10^{12} \text{ s}^{-1}$

$k_{\text{diff}} + k_{\text{react}} \approx k_{\text{react}}$ and $P_{\text{react}} \approx 1$. Thus,

$$R_{\text{LH,diffusion-limit}} = \frac{k_{\text{diff,H}_2} + k_{\text{diff,OH}}}{N_{\text{sites}}} n(\text{H}_2)n(\text{OH}). \quad (6)$$

The other limiting case is a reaction-limited process in which the reaction is much slower than the diffusion of both reactants, *i.e.*, $k_{\text{react}} \ll k_{\text{diff,H}_2} + k_{\text{diff,OH}}$. Then, $P_{\text{react}} \approx k_{\text{react}}/(k_{\text{diff,H}_2} + k_{\text{diff,OH}})$ and

$$R_{\text{LH,reaction-limit}} = \frac{k_{\text{react}}}{N_{\text{sites}}} n(\text{H}_2)n(\text{OH}). \quad (7)$$

Reaction rate constants, like the ones calculated in this work, influence the overall Langmuir–Hinshelwood rate in the general case and in the reaction-limited case. Since H_2 is assumed to diffuse fast, this is likely to be the case for the reaction discussed in this paper.

Usually, for diffusion and desorption the approximation for the rate constant

$$k_{\text{process}} = \nu_{\text{trial}} e^{-E_{\text{process}}/k_{\text{B}}T} \quad (8)$$

is made, where ν_{trial} is the trial frequency and E_{process} the activation energy for diffusion or desorption.

The reaction rate constant k_{react} is provided by our instanton calculations. In models, however, often two approaches are tried and the rate constant that is the highest is chosen to be used in the model run: (a) the rate constant is calculated classically, analogous to equation (8) substituting E_{process} with the reaction barrier and (b) tunneling is taken into account via a semiclassical approximation to the rectangular barrier approximation

$$k_{\text{react}} = \nu_{\text{trial}} e^{-2a/\hbar \sqrt{2\mu E_{\text{reaction}}}}. \quad (9)$$

Here, a is seen as the barrier width, but in fact can not be directly linked to any physical observable and μ is an effective mass. Another way to take into account tunneling is the use of the Eckart barrier approximation instead.

We want to conclude with a specific comparison between values for the reaction rate constants and kinetic isotope effect calculated with the rectangular barrier approximation, the Eckart approximation (all with ν_{trial} kept constant), and instanton theory, taking into account the values published by Furuya et al.²² and Taquet et al.²³ The values for the rate constants and KIE are given in Table 4. Firstly, it is clear that the choice for the value of the

reduced mass has a strong influence on the rate constants and therefore on the KIEs, too. Furthermore, the rectangular barrier approximation is very crude and can underestimate the rate constants by several orders of magnitude. This in turn can lead to wrong predictions of isotope fractionation in the ISM. Moreover, the rate constants themselves also span a large range between the different approaches and parameter choices which can have an effect on the thickness of the ice, the competition of OH reactivity with other species, and on the main route leading to water formation in dense molecular clouds. The Eckart barrier approximation works reasonably for this reaction although the reaction between H and H₂O₂ shows that an order of magnitude difference can appear between rate constants calculated with the Eckart approximation and the instanton method.³⁰ Also the KIEs calculated in this way give surprisingly good agreement with the KIEs obtained with the instanton theory.

With this in mind, we wish to stress that it is important to realize when standard choices of parameter settings such as barrier width and reduced mass may not be enough to describe a reaction properly. In the case where better approximations are available, such as our instanton calculations, k_{react} in equation (5) can directly be taken as the unimolecular rate constant or the fit thereof (see Supplementary Information).

Conclusions

In this study, we computed chemical reaction rate constants of the reaction of hydroxyl radicals with molecular hydrogen (reaction R 9) on an I_h ice surface. For this purpose, we used instanton theory on highly accurate potential energy surfaces. We provide reaction rate constants from 275 K down to 110 K for the ER mechanism (bimolecular) and down to 60 K for the LH mechanism (unimolecular). For both mechanisms, a fit of parameters of a modified Arrhenius equation was performed to obtain a continuous expression of $k(T)$.

To summarize the most important results:

- For the reaction of H₂ and OH radicals, an ice surface just barely influences the potential energy along the reaction path, *i.e.*, there is no classical catalytic effect. Therefore, the surface effects can be included by using an implicit surface model.
- A surface can be implicitly mimicked by a structural gas-phase model, using the same rotational partition function for reactant and transition state. The reaction rate constants obtained in this way differ by a factor of 9.3 from the ones calculated on a full ice surface model.
- We found three different binding sites on our I_h surface. The binding energy lies between 32 and 41 kJ mol⁻¹ (3850 and 4930 K).
- The most important transition state structures and reaction paths are comparable to the ones in the gas phase. It follows that the adiabatic energy barriers (24–25 kJ mol⁻¹) are similar to the barrier of the gas phase reaction (25.4 kJ mol⁻¹, 3055 K).
- Kinetic isotope effects have been calculated for all possible isotope substitution patterns. Exchanging the H to be transferred to D leads to a decrease in the rate constant of 2–3 orders of magnitude. Secondary KIEs are at most half an order of magnitude.

Acknowledgments

This work was financially supported by the German Research Foundation (DFG) within the Cluster of Excellence in Simulation Technology (EXC 310/2) at the University of Stuttgart and the European Union’s Horizon 2020 research and innovation programme (grant agreement No. 646717, TUNNELCHEM). T.L. wishes to acknowledge the Alexander von Humboldt Foundation for generous support. The authors acknowledge support for computer time by the state of Baden-Württemberg through

bwHPC and the Germany Research Foundation (DFG) through grant no INST 40/467-1 FUGG. Marie-Sophie Russ is thanked for assembling the benchmark table and proofreading. Thomas Bissinger is thanked for the initial setup of the QM/MM calculations.

References

- (1) Gillett, F. C.; Forrest, W. J. Spectra of the Becklin-Neugebauer point source and the Kleinmann-Low nebula from 2.8 to 13.5 microns. *Astrophys. J.* **1973**, *179*, 483–491.
- (2) van Dishoeck, E. F. ISO Spectroscopy of Gas and Dust: From Molecular Clouds to Protoplanetary Disks. *Ann. Rev. Astron. Astrophys.* **2004**, *42*, 119.
- (3) Öberg, K. I.; Boogert, A. C. A.; Pontoppidan, K. M.; van den Broek, S.; van Dishoeck, E. F.; Bottinelli, S.; Blake, G. A.; Evans, N. J., II The Spitzer Ice Legacy: Ice Evolution from Cores to Protostars. *Astrophys. J.* **2011**, *740*, 109.
- (4) Boogert, A. A.; Gerakines, P. A.; Whittet, D. C. Observations of the Icy Universe. *Annu. Rev. Astron. Astrophys.* **2015**, *53*, 541–581.
- (5) Hiraoka, K.; Miyagoshi, T.; Takayama, T.; Yamamoto, K.; Kihara, Y. Gas-Grain Processes for the Formation of CH₄ and H₂O: Reactions of H Atoms with C, O, and CO in the Solid Phase at 12 K. *Astrophys. J.* **1998**, *498*, 710–715.
- (6) Miyauchi, N.; Hidaka, H.; Chigai, T.; Nagaoka, A.; Watanabe, N.; Kouchi, A. Formation of hydrogen peroxide and water from the reaction of cold hydrogen atoms with solid oxygen at 10 K. *Chem. Phys. Lett.* **2008**, *456*, 27–30.
- (7) Oba, Y.; Miyauchi, N.; Hidaka, H.; Chigai, T.; Watanabe, N.; Kouchi, A. Formation of Compact Amorphous H₂O Ice by Codeposition of Hydrogen Atoms with Oxygen Molecules on Grain Surfaces. *Astrophys. J.* **2009**, *701*, 464.
- (8) Ioppolo, S.; Cuppen, H. M.; Romanzin, C.; van Dishoeck, E. F.; Linnartz, H. Laboratory Evidence for Efficient Water Formation in Interstellar Ices. *Astrophys. J.* **2008**, *686*, 1474–1479.
- (9) Ioppolo, S.; Cuppen, H. M.; Romanzin, C.; van Dishoeck, E. F.; Linnartz, H. Water formation at low temperatures by surface O₂ hydrogenation I: characterization of ice penetration. *Phys. Chem. Chem. Phys.* **2010**, *12*, 12065–12076.
- (10) Cuppen, H. M.; Ioppolo, S.; Romanzin, C.; Linnartz, H. Water formation at low temperatures by surface O₂ hydrogenation II: the reaction network. *Phys. Chem. Chem. Phys.* **2010**, *12*, 12077–12088.
- (11) Romanzin, C.; Ioppolo, S.; Cuppen, H. M.; van Dishoeck, E. F.; Linnartz, H. Water formation by surface O₃ hydrogenation. *J. Chem. Phys.* **2011**, *134*, 084504.
- (12) Oba, Y.; Osaka, K.; Watanabe, N.; Chigai, T.; Kouchi, A. Reaction kinetics and isotope effect of water formation by the surface reaction of solid H₂O₂ with H atoms at low temperatures. *Faraday Discuss.* **2014**, *168*, 185–204.
- (13) Lamberts, T.; Cuppen, H. M.; Fedoseev, G.; Ioppolo, S.; Chuang, K.-J.; Linnartz, H., Relevance of the H₂ + O reaction pathway for the surface formation of interstellar water. *Astron. Astrophys.* **2014**, *570*, A57.
- (14) Lamberts, T.; Fedoseev, G.; Puletti, F.; Ioppolo, S.; Cuppen, H. M.; Linnartz, H. Low-temperature chemistry between water and hydroxyl radicals: H/D isotopic effects. *Mon. Not. R. Astron. Soc.* **2016**, *455*, 634–641.

- (15) Hama, T.; Kouchi, A.; Watanabe, N. Statistical ortho-to-para ratio of water desorbed from ice at 10 kelvin. *Science* **2016**, *351*, 65–67.
- (16) Cuppen, H. M.; Herbst, E. Simulation of the Formation and Morphology of Ice Mantles on Interstellar Grains. *Astrophys. J.* **2007**, *668*, 294.
- (17) Chang, Q.; Cuppen, H. M.; Herbst, E. Gas-grain chemistry in cold interstellar cloud cores with a microscopic Monte Carlo approach to surface chemistry. *Astron. Astrophys.* **2007**, *469*, 973–983.
- (18) Cazaux, S.; Cobut, V.; Marseille, M.; Spaans, M.; Caselli, P. Water formation on bare grains: When the chemistry on dust impacts interstellar gas. *Astron. Astrophys.* **2010**, *522*, A74.
- (19) Garrod, R. T. A Three-phase Chemical Model of Hot Cores: The Formation of Glycine. *Astrophys. J.* **2013**, *765*, 60.
- (20) Vasyunin, A. I.; Herbst, E. A Unified Monte Carlo Treatment of Gas-Grain Chemistry for Large Reaction Networks. II. A Multiphase Gas-Surface-Layered Bulk Model. *Astrophys. J.* **2013**, *762*, 86.
- (21) Lamberts, T.; de Vries, X.; Cuppen, H. M. The formation of ice mantles on interstellar grains revisited - the effect of exothermicity. *Faraday Discuss.* **2014**, *168*, 327–347.
- (22) Furuya, K.; Aikawa, Y.; Nomura, H.; Hersant, F.; Wakelam, V. Water in Protoplanetary Disks: Deuteration and Turbulent Mixing. *Astrophys. J.* **2013**, *779*, 11.
- (23) Taquet, V.; Peters, P. S.; Kahane, C.; Ceccarelli, C.; López-Sepulcre, A.; Toubin, C.; DufLOT, D.; Wiesenfeld, L., Water ice deuteration: a tracer of the chemical history of protostars. *Astron. Astrophys.* **2013**, *550*, A127.
- (24) Furuya, K.; Drozdovskaya, M. N.; Visser, R.; van Dishoeck, E. F.; Walsh, C.; Harsono, D.; Hincelin, U.; Taquet, V., Water delivery from cores to disks: Deuteration as a probe of the prestellar inheritance of H₂O. *Astron. Astrophys.* **2017**, *599*, A40.
- (25) Bukas, V. J.; Mitra, S.; Meyer, J.; Reuter, K. Fingerprints of energy dissipation for exothermic surface chemical reactions: O₂ on Pd(100). *J. Chem. Phys.* **2015**, *143*, 034705.
- (26) van Dishoeck, E. F.; Herbst, E.; Neufeld, D. A. Interstellar Water Chemistry: From Laboratory to Observations. *Chem. Rev.* **2013**, *113*, 9043–9085.
- (27) Tielens, A.; Hagen, W. Model calculations of the molecular composition of interstellar grain mantles. *Astron. Astrophys.* **1982**, *114*, 245–260.
- (28) Dulieu, F.; Amiaud, L.; Congiu, E.; Fillion, J.-H.; Matar, E.; Momeni, A.; Pirronello, V.; Lemaire, J. L., Experimental evidence for water formation on interstellar dust grains by hydrogen and oxygen atoms. *Astron. Astrophys.* **2010**, *512*, A30.
- (29) Jing, D.; He, J.; Brucato, J.; Sio, A. D.; Tozzetti, L.; Vidali, G. On Water Formation in the Interstellar Medium: Laboratory Study of the O+D Reaction on Surfaces. *Astrophys. J. Lett.* **2011**, *741*, L9.
- (30) Lamberts, T.; Samanta, P. K.; Köhn, A.; Kästner, J. Quantum tunneling during interstellar surface-catalyzed formation of water: the reaction $\text{H} + \text{H}_2\text{O}_2 \rightarrow \text{H}_2\text{O} + \text{OH}$. *Phys. Chem. Chem. Phys.* **2016**, *18*, 33021–33030.
- (31) Keyser, L. F. Absolute rate constant and branching fractions for the atomic hydrogen + hydroperoxyl radical reaction from 245 to 300 K. *J. Phys. Chem.* **1986**, *90*, 2994–3003.

- (32) Mousavipour, S. H.; Fernández-Ramos, A.; Meana-Pañeda, R.; Martínez-Núñez, E.; Vázquez, S. A.; Ríos, M. A. Direct-Dynamics VTST Study of the [1,7] Hydrogen Shift in 7-Methylocta-1,3(Z),5(Z)-triene. A Model System for the Hydrogen Transfer Reaction in Previtamin D3. *J. Phys. Chem. A* **2007**, *111*, 719–725.
- (33) Lamberts, T.; Cuppen, H. M.; Ioppolo, S.; Linnartz, H. Water formation at low temperatures by surface O₂ hydrogenation III: Monte Carlo simulation. *Phys. Chem. Chem. Phys.* **2013**, *15*, 8287–8302.
- (34) Mokrane, H.; Chaabouni, H.; Accolla, M.; Congiu, E.; Dulieu, F.; Chehrouri, M.; Lemaire, J. L. Experimental Evidence for Water Formation Via Ozone Hydrogenation on Dust Grains at 10 K. *Astrophys. J. Lett.* **2009**, *705*, L195.
- (35) Ravishankara, A. R.; Nicovich, J. M.; Thompson, R. L.; Tully, F. P. Kinetic study of the reaction of hydroxyl with hydrogen and deuterium from 250 to 1050 K. *J. Phys. Chem.* **1981**, *85*, 2498–2503.
- (36) Talukdar, R. K.; Gierczak, T.; Goldfarb, L.; Rudich, Y.; Rao, B. S. M.; Ravishankara, A. R. Kinetics of Hydroxyl Radical Reactions with Isotopically Labeled Hydrogen. *J. Phys. Chem.* **1996**, *100*, 3037–3043.
- (37) Orkin, V. L.; Kozlov, S. N.; Poskrebyshv, G. A.; Kurylo, M. J. Rate Constant for the Reaction of OH with H₂ between 200 and 480 K. *J. Phys. Chem. A* **2006**, *110*, 6978–6985.
- (38) Matzkies, F.; Manthe, U. Accurate quantum calculations of thermal rate constants employing MCTDH: H₂ + OH → H + H₂O and D₂ + OH → D + DOH. *J. Chem. Phys.* **1998**, *108*, 4828–4836.
- (39) Manthe, U.; Matzkies, F. Rotational effects in the H₂ + OH → H + H₂O reaction rate: Full-dimensional close-coupling results. *J. Chem. Phys.* **2000**, *113*, 5725–5731.
- (40) Nguyen, T. L.; Stanton, J. F.; Barker, J. R. A practical implementation of semi-classical transition state theory for polyatomics. *Chem. Phys. Lett.* **2010**, *499*, 9 – 15.
- (41) Nguyen, T. L.; Stanton, J. F.; Barker, J. R. Ab Initio Reaction Rate Constants Computed Using Semi-classical Transition-State Theory: HO + H₂ → H₂O + H and Isotopologues. *J. Phys. Chem. A* **2011**, *115*, 5118–5126.
- (42) Meisner, J.; Kästner, J. Reaction Rates and Kinetic Isotope Effects of H₂ + OH → H₂O + H. *J. Chem. Phys.* **2016**, *144*, 174303.
- (43) Atkinson, R.; Baulch, D. L.; Cox, R. A.; Crowley, J. N.; Hampson, R. F.; Hynes, R. G.; Jenkin, M. E.; Rossi, M. J.; Troe, J. Evaluated kinetic and photochemical data for atmospheric chemistry: Volume I - gas phase reactions of O_x, HO_x, NO_x and SO_x species. *Atmos. Chem. Phys.* **2004**, *4*, 1461–1738.
- (44) Oba, Y.; Watanabe, N.; Hama, T.; Kuwahata, K.; Hidaka, H.; Kouchi, A. Water Formation through a Quantum Tunneling Surface Reaction, OH + H₂, at 10 K. *Astrophys. J.* **2012**, *749*, 67.
- (45) Adler, T. B.; Knizia, G.; Werner, H.-J. A simple and efficient CCSD(T)-F12 approximation. *J. Chem. Phys.* **2007**, *127*, 221106.
- (46) Adler, T. B.; Werner, H.-J. Local explicitly correlated coupled-cluster methods: Efficient removal of the basis set incompleteness and domain errors. *J. Chem. Phys.* **2009**, *130*, 241101.
- (47) Langer, J. S. Theory of the condensation point. *Ann. Phys. (N.Y.)* **1967**, *41*, 108.

- (48) Miller, W. H. Semiclassical limit of quantum mechanical transition state theory for nonseparable systems. *J. Chem. Phys.* **1975**, *62*, 1899.
- (49) Coleman, S. Fate of the false vacuum: Semiclassical theory. *Phys. Rev. D* **1977**, *15*, 2929.
- (50) Callan Jr., C. G.; Coleman, S. Fate of the false vacuum. II. First quantum corrections. *Phys. Rev. D* **1977**, *16*, 1762.
- (51) Gildener, E.; Patrascioiu, A. Pseudoparticle contributions to the energy spectrum of a one-dimensional system. *Phys. Rev. D* **1977**, *16*, 423.
- (52) Dirac, P. Quantum Mechanics of Many-Electron Systems. *Proc. Royal Soc. (London) A* **1929**, *123*, 714.
- (53) Slater, J. A simplification of the Hartree-Fock method. *Phys. Rev.* **1951**, *81*, 385.
- (54) Becke, A. Density-functional exchange-energy approximation with correct asymptotic behavior. *Phys. Rev. A* **1988**, *38*, 3098.
- (55) Lee, C.; Yang, W.; Parr, R. G. Development of the Colle-Salvetti correlation-energy formula into a functional of the electron density. *Phys. Rev. B* **1988**, *37*, 785–789.
- (56) Becke, A. D. A new mixing of Hartree-Fock and local density-functional theories. *J. Chem. Phys.* **1993**, *98*, 1372–1377.
- (57) Rappoport, D.; Furche, F. Property-optimized Gaussian basis sets for molecular response calculations. *J. Chem. Phys.* **2010**, *133*.
- (58) Andersson, S.; Grüning, M. Performance of Density Functionals for Calculating Barrier Heights of Chemical Reactions Relevant to Astrophysics. *J. Phys. Chem. A* **2004**, *108*, 7621–7636.
- (59) Rimola, A.; Taquet, V.; Ugliengo, P.; Balucani, N.; Ceccarelli, C. Combined quantum chemical and modeling study of CO hydrogenation on water ice. *Astron. Astrophys.* **2014**, *572*, A70.
- (60) TURBOMOLE V7.0.1 2015, a development of University of Karlsruhe and Forschungszentrum Karlsruhe GmbH, 1989-2007, TURBOMOLE GmbH, since 2007; available from <http://www.turbomole.com>.
- (61) Eichkorn, K.; Weigend, F.; Treutler, O.; Ahlrichs, R. Auxiliary basis sets for main row atoms and transition metals and their use to approximate Coulomb potentials. *Theor. Chem. Acc.* **1997**, *97*, 119–124.
- (62) Sherwood, P. et al. QUASI: A general purpose implementation of the QM/MM approach and its application to problems in catalysis. *J. Mol. Struct. (THEOCHEM)* **2003**, *632*, 1.
- (63) Metz, S.; Kästner, J.; Sokol, A. A.; Keal, T. W.; Sherwood, P. ChemShell—a modular software package for QM/MM simulations. *WIREs Comput. Mol. Sci.* **2014**, *4*, 101.
- (64) Kästner, J.; Carr, J. M.; Keal, T. W.; Thiel, W.; Wander, A.; Sherwood, P. DL-FIND: an Open-Source Geometry Optimizer for Atomistic Simulations. *J. Phys. Chem. A* **2009**, *113*, 11856.
- (65) Humphrey, W.; Dalke, A.; Schulten, K. VMD: Visual molecular dynamics. *J. Mol. Graph.* **1996**, *14*, 33 – 38.
- (66) Fletcher, N. H. Reconstruction of ice crystal surfaces at low temperatures. *Philos. Mag. Part B* **1992**, *66*, 109–115.
- (67) Jorgensen, W. L.; Chandrasekhar, J.; Madura, J. D.; Impey, R. W.; Klein, M. L. Comparison of simple potential functions for simulating liquid water. *J. Chem. Phys.* **1983**, *79*, 926.

- (68) Affleck, I. Quantum-Statistical Metastability. *Phys. Rev. Lett.* **1981**, *46*, 388–391.
- (69) Coleman, S. Quantum Tunneling and negative Eigenvalues. *Nucl. Phys. B* **1988**, *298*, 178.
- (70) Hänggi, P.; Talkner, P.; Borkovec, M. Reaction-rate theory: fifty years after Kramers. *Rev. Mod. Phys.* **1990**, *62*, 251.
- (71) Benderskii, V. A.; Makarov, D. E.; Wight, C. A. One-Dimensional Models. *Adv. Chem. Phys.* **1994**, *88*, 55.
- (72) Messina, M.; Schenter, G. K.; Garrett, B. C. A variational centroid density procedure for the calculation of transmission coefficients for asymmetric barriers at low temperature. *J. Chem. Phys.* **1995**, *103*, 3430.
- (73) Richardson, J. O.; Althorpe, S. C. Ring-polymer molecular dynamics rate-theory in the deep-tunneling regime: Connection with semiclassical instanton theory. *J. Chem. Phys.* **2009**, *131*, 214106.
- (74) Althorpe, S. C. On the equivalence of two commonly used forms of semiclassical instanton theory. *J. Chem. Phys.* **2011**, *134*, 114104.
- (75) Rommel, J. B.; Goumans, T. P. M.; Kästner, J. Locating instantons in many degrees of freedom. *J. Chem. Theory Comput.* **2011**, *7*, 690.
- (76) Rommel, J. B.; Kästner, J. Adaptive Integration Grids in Instanton Theory Improve the Numerical Accuracy at Low Temperature. *J. Chem. Phys.* **2011**, *134*, 184107.
- (77) Richardson, J. O. Derivation of instanton rate theory from first principles. *J. Chem. Phys.* **2016**, *144*.
- (78) Feynman, R. P. Space-Time Approach to Non-Relativistic Quantum Mechanics. *Rev. Mod. Phys.* **1948**, *20*, 367.
- (79) Kästner, J. Theory and Simulation of Atom Tunneling in Chemical Reactions. *WIREs Comput. Mol. Sci.* **2014**, *4*, 158.
- (80) Chapman, S.; Garrett, B. C.; Miller, W. H. Semiclassical transition state theory for nonseparable systems: Application to the collinear H+H₂ reaction. *J. Chem. Phys.* **1975**, *63*, 2710.
- (81) Mills, G.; Jónsson, H. Quantum and thermal effects in H₂ dissociative adsorption: Evaluation of free energy barriers in multidimensional quantum systems. *Phys. Rev. Lett.* **1994**, *72*, 1124.
- (82) Mills, G.; Jónsson, H.; Schenter, G. K. Reversible work transition state theory: application to dissociative adsorption of hydrogen. *Surf. Sci.* **1995**, *324*, 305–337.
- (83) Mills, G.; Schenter, G. K.; Makarov, D. E.; Jónsson, H. Generalized path integral based quantum transition state theory. *Chem. Phys. Lett.* **1997**, *278*, 91.
- (84) Siebrand, W.; Smedarchina, Z.; Zgierski, M. Z.; Fernández-Ramos, A. Proton tunnelling in polyatomic molecules: A direct-dynamics instanton approach. *Int. Rev. Phys. Chem.* **1999**, *18*, 5.
- (85) Smedarchina, Z.; Siebrand, W.; Fernández-Ramos, A.; Cui, Q. Kinetic Isotope Effects for Concerted Multiple Proton Transfer: A Direct Dynamics Study of an Active-Site Model of Carbonic Anhydrase II. *J. Am. Chem. Soc.* **2003**, *125*, 243–251.
- (86) Qian, T.; Ren, W.; Shi, J.; E, W.; Shen, P. Numerical study of metastability due to tunneling: The quantum string method. *Physica A* **2007**, *379*, 491.
- (87) Andersson, S.; Nyman, G.; Arnaldsson, A.; Manthe, U.; Jónsson, H. Comparison of Quantum Dynamics and

- Quantum Transition State Theory Estimates of the $\text{H} + \text{CH}_4$ Reaction Rate. *J. Phys. Chem. A* **2009**, *113*, 4468.
- (88) Goumans, T. P. M.; Andersson, S. Tunneling in the $\text{O} + \text{CO}$ reaction. *Mon. Not. R. Astron. Soc.* **2010**, *406*, 2213–2217.
- (89) Goumans, T. P. M. Hydrogen chemisorption on polycyclic aromatic hydrocarbons via tunnelling. *Mon. Not. Roy. Astron. Soc.* **2011**, *415*, 3129–3134.
- (90) Goumans, T. P. M. Isotope effects for formaldehyde plus hydrogen addition and abstraction reactions: rate calculations including tunnelling. *Mon. Not. Roy. Astron. Soc.* **2011**, *413*, 26150–2620.
- (91) Goumans, T. P. M.; Kästner, J. Hydrogen-Atom Tunneling Could Contribute to H_2 Formation in Space. *Angew. Chem. Int. Ed.* **2010**, *49*, 7350–7352.
- (92) Jónsson, H. Simulation of surface processes. *Proc. Nat. Acad. Sci. U.S.A.* **2010**, *108*, 944–949.
- (93) Meisner, J.; Rommel, J. B.; Kästner, J. Kinetic Isotope Effects Calculated with the Instanton Method. *J. Comput. Chem.* **2011**, *32*, 3456.
- (94) Goumans, T. P. M.; Kästner, J. Deuterium Enrichment of Interstellar Methanol Explained by Atom Tunneling. *J. Phys. Chem. A* **2011**, *115*, 10767.
- (95) Einarsson, D. M.; Arnaldsson, A.; Óskarsson, F.; Jónsson, H. Path optimization with application to tunneling. *Lect. Notes Comput. Sci.* **2012**, *7134*, 45.
- (96) Rommel, J. B.; Liu, Y.; Werner, H.-J.; Kästner, J. Role of Tunneling in the Enzyme Glutamate Mutase. *J. Phys. Chem. B* **2012**, *116*, 13682.
- (97) Kryvohuz, M.; Marcus, R. A. Semiclassical evaluation of kinetic isotope effects in 13-atomic system. *J. Chem. Phys.* **2012**, *137*, 134107.
- (98) Kästner, J. The Path Length Determines the Tunneling Decay of Substituted Carbenes. *Chem. Eur. J.* **2013**, *19*, 8207–8212.
- (99) Álvarez-Barcia, S.; Flores, J. R.; Kästner, J. Tunneling Above the Crossover Temperature. *J. Phys. Chem. A* **2014**, *118*, 78.
- (100) Kryvohuz, M. Calculation of Kinetic Isotope Effects for Intramolecular Hydrogen Shift Reactions Using Semiclassical Instanton Approach. *J. Phys. Chem. A* **2014**, *118*, 535–544.
- (101) Song, L.; Kästner, J. Formation of the prebiotic molecule NH_2CHO on astronomical amorphous solid water surfaces: accurate tunneling rate calculations. *Phys. Chem. Chem. Phys.* **2016**, *18*, 29278–29285.
- (102) Álvarez-Barcia, S.; Russ, M.-S.; Meisner, J.; Kästner, J. Atom tunnelling in the reaction $\text{NH}_3^+ + \text{H}_2 \rightarrow \text{NH}_4^+ + \text{H}$ and its astrochemical relevance. *Faraday Disc.* **2016**, *195*, 69–80.
- (103) Lamberts, T.; Fedoseev, G.; Kästner, J.; Ioppolo, S.; Linnartz, H., Importance of tunneling in H-abstraction reactions by OH radicals - The case of $\text{CH}_4 + \text{OH}$ studied through isotope-substituted analogs. *Astron. Astrophys.* **2017**, *599*, A132.
- (104) Kobayashi, H.; Hidaka, H.; Lamberts, T.; Hama, T.; Kawakita, H.; Kästner, J.; Watanabe, N. Hydrogenation and Deuteration of C_2H_2 and C_2H_4 on Cold Grains: A Clue to the Formation Mechanism of C_2H_6 with Astronomical Interest. *Astrophys. J.* **2017**, *837*, 155.
- (105) Fernández-Ramos, A.; Ellingson, B. A.; Meana-Pañeda, R.; Marques, J. M. C.; Truhlar, D. G. Symmetry numbers and

- chemical reaction rates. *Theor. Chem. Acc.* **2007**, *118*, 813–826.
- (106) McConnell, S. R.; Löhle, A.; Kästner, J. Rate constants from instanton theory via a microcanonical approach. *J. Chem. Phys.* **2017**, *146*, 074105.
- (107) Hratchian, H. P.; Schlegel, H. B. Accurate reaction paths using a Hessian based predictor–corrector integrator. *J. Chem. Phys.* **2004**, *120*, 9918.
- (108) Hratchian, H. P.; Schlegel, H. B. Using Hessian Updating To Increase the Efficiency of a Hessian Based Predictor-Corrector Reaction Path Following Method. *J. Chem. Theory Comput.* **2005**, *1*, 61–69.
- (109) Meisner, J.; Markmeyer, M. N.; Bohner, M. U.; Kästner, J. Comparison of Classical Reaction Paths and Tunneling Paths studied by the Semi-classical Instanton Theory. *J. Chem. Theory Comput.*, submitted **2017**,
- (110) He, J.; Vidali, G. Experiments of Water Formation on Warm Silicates. *Astrophys. J.* **2014**, *788*, 50.
- (111) Cuppen, H. M.; Walsh, C.; Lamberts, T.; Semenov, D.; Garrod, R. T.; Penteado, E. M.; Ioppolo, S. Grain Surface Models and Data for Astrochemistry. *Space Sci. Rev.* **2017**, 1–58.
- (112) Pérez de Tudela, R.; Aoiz, F. J.; Suleimanov, Y. V.; Manolopoulos, D. E. Chemical Reaction Rates from Ring Polymer Molecular Dynamics: Zero Point Energy Conservation in $\text{Mu} + \text{H}_2 \rightarrow \text{MuH} + \text{H}$. *J. Phys. Chem. Lett.* **2012**, *3*, 493–497.
- (113) Suleimanov, Y. V.; de Tudela, R. P.; Jambrina, P. G.; Castillo, J. F.; Sáez-Rábanos, V.; Manolopoulos, D. E.; Aoiz, F. J. A ring polymer molecular dynamics study of the isotopologues of the $\text{H} + \text{H}_2$ reaction. *Phys. Chem. Chem. Phys.* **2013**, *15*, 3655–3665.
- (114) Pérez de Tudela, R.; Suleimanov, Y. V.; Richardson, J. O.; Rábanos, V. S.; Green, W. H.; Aoiz, F. J. Stress Test for Quantum Dynamics Approximations: Deep Tunneling in the Muonium Exchange Reaction $\text{D} + \text{HMu} \rightarrow \text{DMu} + \text{H}$. *J. Phys. Chem. Lett.* **2014**, *5*, 4219–4224.
- (115) Meisner, J.; Kästner, J. Atom-Tunneling in Chemistry. *Angew. Chem. Int. Ed.* **2016**, *55*, 5400–5413.
- (116) Zheng, J.; Truhlar, D. G. Kinetics of hydrogen-transfer isomerizations of butoxyl radicals. *Phys. Chem. Chem. Phys.* **2010**, *12*, 7782–7793.
- (117) Chang, Q.; Herbst, E. Interstellar Simulations Using a Unified Microscopic-Macroscopic Monte Carlo Model with a Full Gas-Grain Network Including Bulk Diffusion in Ice Mantles. *Astrophys. J.* **2014**, *787*, 135.